Tissue folding at the organ-meristem boundary results in nuclear compression and chromatin compaction

K. Fal, Niklas Korsbo, Juan Alonso-Serra, Jose Teles, Mengying Liu, Yassin Refahi, M-E. Chabouté, Henrik Jönsson, Olivier Hamant

Classification: Biological sciences, Plant biology, biophysics and computational biology

Title: Tissue folding at the organ-meristem boundary results in nuclear compression and chromatin compaction

Authors: Kateryna Fal[1,2,3]*, Niklas Korsbo[4,5]†, Juan Alonso-Serra[1]†, Jose Teles[4]†, Mengying Liu[1], Yassin Refahi[4,6], Marie-Edith Chabouté[7], Henrik Jönsson[2,4,5]*, Olivier Hamant[1]*

Affiliations:

[1]Laboratoire de Reproduction et Développement des Plantes, Université de Lyon, UCB Lyon 1, ENS de Lyon, INRA, CNRS, 46 Allée d'Italie, 69364 Lyon Cedex 07, France

[2]Department of Astronomy and Theoretical Physics, Lund University, Sölvegatan 14A, SE22362 Lund, Sweden

[3]Laboratoire Physiologie Cellulaire & Végétale, Institut de Biosciences et de Biotechnologie de Grenoble, CEA-Grenoble, 17 avenue des Martyrs, 38054 Grenoble cedex 9, France

[4]Sainsbury Laboratory, University of Cambridge, Bateman Street, Cambridge CB2 1LR, UK.

[5]Department of Applied Mathematics and Theoretical Physics, University of Cambridge, Cambridge, UK.

[6]Université de Reims Champagne Ardenne, INRAE, FARE, UMR A 614, 51097 Reims, France

[7]Institut de biologie moléculaire des plantes, CNRS, Université de Strasbourg, 12, rue du Général Zimmer, 67084, Strasbourg Cedex, France.

*Correspondence to: kateryna.fal@cea.fr; henrik.jonsson@slcu.cam.ac.uk, olivier.hamant@ens-lyon.fr

† equal contributions

Keywords: nucleus, mechanical forces, meristem, organogenesis, chromatin, Arabidopsis

Abstract:

Artificial mechanical perturbations affect chromatin in animal cells in culture. Whether this is also relevant to growing tissues in living organisms remains debated. In plants, aerial organ emergence occurs through localized outgrowth at the periphery of the shoot apical meristem, which also contains a stem cell niche. Interestingly, organ outgrowth has been proposed to generate compression in the saddle-shaped organ-meristem boundary domain. Yet, whether such growth-induced mechanical stress affects chromatin in plant tissues is unknown. Here, by imaging the nuclear envelope *in vivo* over time and quantifying nucleus deformation, we demonstrate the presence of active nuclear compression in that domain. We developed a quantitative pipeline amenable to identify a subset of very deformed nuclei deep in the boundary, and in which nuclei become gradually narrower and more elongated as the cell contracts transversely. In this domain, we find that the number of chromocenters is reduced, as shown by chromatin staining and labeling, and that the expression of linker histone H1.3 is induced. As further evidence of the role of forces on chromatin changes, artificial compression with a microvice could induce the ectopic induction of H1.3 in the rest of the meristem. Furthermore, while the methylation status of chromatin was correlated with nucleus deformation at the meristem boundary, such correlation was lost in the *h1.3* mutant. Altogether, we reveal that organogenesis in plants generates compression that is able to have global effects on chromatin in individual cells.

Significance statement: During development, growth deforms tissues and organs. This is notably the case during the formation of new flowers in plants, as the tissue folds during young floral bud emergence. Here we provide further evidence that organogenesis compresses the cells at the boundary separating the organ from the stem cell niche, and we show that this leads to nucleus compression and chromatin changes. While mechanical forces are well known to affect nucleus shape and chromatin in Mammalian cells in culture, this demonstrates that such effect also occurs in a developing organism, and suggests that forces may help to define boundary domains through large-scale chromatin effects.

Introduction

Forces act as instructive mechanical signals that affect all aspects of cell and developmental biology (1)(2). Although much attention has been paid to the role of forces at the cell cortex, forces can also propagate to the nucleus, and affect chromatin and gene expression (3)(4)(5)(6). In turn, chromatin changes can also affect nucleus stiffness and shape (7). However, the impact of forces on nuclei has mainly been studied in single cell systems using artificial micromechanical manipulations so far. Patterns of forces are naturally present in multicellular tissues. In particular, mechanical conflicts result from differential growth and tissue morphogenesis (e.g. (8)(9)). In plants, because cells are encaged in a wall, cell movement is hindered; when tissues grow and change their shape, cells have to cope with the resulting mechanical stress, without resolving to cell intercalation (nor cell death in young tissues). In Arabidopsis shoot apical meristems, tissue folding occurs at the boundary between organs and meristem. Finite element model simulations suggest that this domain experiences highly anisotropic tension in the circumferential direction or radial compression (10). Radial contraction of the outer cell wall has been reported in that domain in previous studies and would be consistent with compression at the boundary (11). Here, we characterized the nuclear compression at the organ boundary correlating with changes of chromatin organization and linker histone H1.3 activity.

Results

Nuclei become elongated as the organ-meristem boundary folds

Using *pPDF1::CFP-N7* marker line, which marks nuclei (N7 nuclear localization signal) in the epidermis (PDF1 promoter), we observed that some nuclei at the boundary often display an elongated shape (Fig. 1A). These elongated nuclei appeared late in boundary formation, i.e. when tissue folding is pronounced (i.e. beyond flower stage 2, (12)) and when major supracellular alignment of cortical microtubules is observed (Fig. 1A). When staining with FM4-64, we observed that these nuclei might be physically constrained by cell geometry (as the

nuclear-cytoplasmic ratio is high in meristematic cells, Fig. 1A), consistent with predicted compression in that domain (13)(10).

Because cell division follows the direction of maximal tension, cells at the boundary divide along one of their long axes (14). Therefore, cells appear more elongated in that domain. In principle, this may be sufficient to constrain nucleus shape. However, in that scenario, the presence of elongated nuclei would not be the result of progressive compression emerging from neighboring tissue growth. To check whether organ growth can indeed actively compress nuclei at the boundary, we used the *p35S::SUN1-YFP* line (with *SUN1* for *SAD1/UNC-84 DOMAIN PROTEIN 1*) that marks the nuclear envelope (15) and followed nuclear behavior in non-dividing cells every 12 hours. We could identify a population of non-dividing cells that exhibit progressive nucleus deformation (Fig. 1B, C). The magnitude of nucleus deformation increased with tissue curvature, consistent with organ growth being the main cause for nuclear compression in these cells (Fig. 1B, C). In fact, we could mimic such nucleus deformation by mechanically compressing shoot apices laterally in a microvice with a force of ca. 0.1N (see SI Appendix, Fig. S1). Altogether, this suggests that nuclear deformation in the boundary region is the result of compressive stresses caused by organ outgrowth.

To quantify these nuclear phenotypes, we used images obtained with the *p35S::SUN1-YFP* line and developed a computational pipeline to track cells and nuclei and quantify nuclear shapes (see SI Appendix, Fig. S2). In brief, MorphoGraphX (16) was used to extract the meristem surface, and segment (2D) cells on which the curvature was mapped. In addition, 3D cell segmentation of the epidermal layer followed by cell tracking was performed using MARS/ALT (17). The nuclei were segmented in 3D using the MARS watershed algorithm. Finally, meristem regions and nuclear shapes were extracted and quantified using MATLAB (The MathWorks, Inc., Natick, Massachusetts, United States) scripts, after projecting the nuclear signal in 2D.

A subpopulation of nuclei at the boundary region exhibited a significant increase in their aspect-ratio. In each boundary we could find a group of at least 10 nuclei with an aspect ratio superior to 1.55, whereas meristematic nuclei typically have an aspect ratio of 1.2 +/- 0.15 (n=132) (Fig. 2A, see SI Appendix, Fig. S3, S4). When backtracking these most affected nuclei *via* their cell

lineages, we also found that they increased their aspect ratio following the increased growth of the primordia, correlating with the increased (negative) curvature of the boundary domain (Fig. 2B-C, see SI Appendix, Fig. S3, S4). Altogether, these quantifications demonstrate the existence of active nucleus compression operating at the meristem boundary during organogenesis and highlight the presence of a subset of boundary cells with increasing negative curvature in time, indicative of cellular compression.

Linker histone H1.3 is induced by compression

The boundary domain has a specific gene expression profile (18). This pattern relies on hormones, microRNA and mechanical stress (19)(20)(21). Nucleus compression is likely to have a more global effect on chromatin, than on specific gene expression, as shown in animal systems (22)(23)(5)(6). Furthermore, changes in global chromatin state have been associated with changes in chromatin compaction, which relies on linker histones (H1 isoforms). In plants, at least 3 isoforms of H1 have been studied. Their expression and competitive binding to DNA depend on cell cycle as well as on external stress factors. H1.3 has been associated with the cell's response to abiotic stresses in past work (24). In particular, H1.3 is induced by drought stress (24), which, based on data from animals (e.g. (25)(26)), might also drive nucleus compaction. When analyzing the expression pattern of three variants of histone H1 in the meristem, we found that H1.1 and H1.2 were expressed in the entire meristem, with a higher expression level in organs. Interestingly, H1.3 exhibited a patchy pattern, with the strongest signal deep in meristem boundaries (Fig. 3A). To go beyond this correlation, we next applied compression on meristem to check whether H1.3 expression would be induced. To do so, we used NPA-treated seedlings and placed the naked stems between two blades of the microvice (see SI Appendix, Fig. S1A, see material and methods). When the blades were touching the meristem without deforming it, no clear H1.3 expression could be detected in the meristem (Fig. 3B, see SI Appendix, Fig. S5B, n=6/6 meristems with less than 3 nuclei exhibiting H1.3 induction at t=8h). However, when the meristem was deformed upon compression, most meristems expressed H1.3 ectopically (Fig. 3B, see SI Appendix, Fig. S5B, n=10/11 meristems with more than 3 nuclei exhibiting H1.3 induction at t=8h). Our finding suggests that cells at the meristem boundary are experiencing high and long enough compressive stress to induce such expression.

Global chromatin changes occur at the organ-meristem boundary

Our results suggest that nuclear compression, naturally occurring during organogenesis, generates iterative chromatin changes each time a new organ emerges. To further test this hypothesis, we investigated whether nucleus compression is strong enough to affect chromatin architecture. To do so, we used whole-mount fixed meristems and stained them with DAPI, which displays brighter signal in heterochromatin regions corresponding to chromocenters (e.g. (27)). We analyzed their distribution in successive optical sections (see SI Appendix, Fig. S6A). To check whether nucleus compression affects the distribution of these chromocenters, we compared nuclei with an aspect ratio superior or inferior to 1.55, which corresponds to the threshold identifying the significantly most deformed nuclei (cf. Fig. 2B). We observed that the number of chromocenters decreased in more compressed nuclei (see SI Appendix, Fig. S6B, *p*-value = 8.2×10^{-10}, two-tailed Student's t-test). To further confirm this result, we used a *pHTR5::mCG-MBD-GFP* line (MBD for Methyl-CpG Binding Domain, (28)(29)(30)), which marks CG methylation (a marker of heterochromatin, Fig. 4A,B). Consistent with our previous results on the DAPI stained meristems, we detected a decrease in the number of mCG regions within the nuclei with the higher aspect ratio (Fig. 4C,D, *p*-value = 7.3×10^{-5}, two-tailed Student's t-test). These results indicate that nuclei compression at the organ boundary colocalizes with modifications of chromatin architecture.

In isolated human umbilical vein endothelial cells, the average nuclear signal density changes as a function of the nuclear shape and is higher in the most elongated nuclei (31). Therefore, we tested the correlation of the average nuclear signal density and the nuclear aspect ratio. Consistently with the reported data on human cells, we detected an increase in average nuclear signal density in the nuclei with the higher aspect ratio (Fig. 4E, *p*-value = 4.5×10^{-8}, two-tailed Student's t-test; see SI Appendix, Fig. S6C).

Last, to check whether the induction of H1.3 in deformed nuclei could be associated with such global chromatin changes, we analyzed the nuclei of the *h1.3* mutant. The size and shapes of the *h1.3* nuclei in the boundary domain were not significantly affected (Fig. 5A,B). Similarly, the

number of chromocenters appeared comparable in wild type and *h1.3* mutant at the boundary (see SI Appendix, Fig. S7A). In line with previous analyses of whole plant CHH DNA methylation in *h1.3* (24), we introgressed the *pHTR5::mCHH-GFP* reporter into *h1.3* plants to further analyze the role of H1.3 in the nuclei at the organ boundary. We detected induction of the signal density (normalized signal of the CHH) in the WT nuclei with the aspect ratio above 1.55 but not in those of *h1.3* (Fig. 5C, $p\text{-value}_{wt} = 1.35\times10^{-5}$; $p\text{-value}_{h1.3} = 0.1$, two-tailed Student's t-test; see SI Appendix, Fig. S7B and S7C), thereby suggesting that H1.3 is required for DNA methylation changes at the organ boundary.

Discussion

We show that organogenesis at the shoot apical meristem leads to nucleus compression in a specific set of cells, which is accompanied by major chromatin changes. This demonstrates that forces have a strong and direct impact on nuclei in a tissue context. The role of forces on chromatin is now well established, notably through experiments with artificial deformations of single cells in culture (4)(5)(6). Our results not only show that such effects also occur in plants, but they also demonstrate that these effects occur in the natural context of a developing organ. In fact, several reports have proposed that the main role of forces in the nucleus is to affect the physics of chromatin, which in turn would affect gene expression (instead of affecting specific genes that would then affect chromatin). For instance, nuclei have been found to exhibit an auxetic behavior, because of the decompaction of chromatin upon nucleus stretching (7). Our results are consistent with such conceptual framework and suggest that forces may primarily have global effects on chromatin, which would thus subsequently affect the expression of specific genes.

In previous work, we had already shown that *STM* and *CUC3* are induced by mechanical stress at the organ-meristem boundary (20)(21). However, both of these genes are induced in shallow boundaries, i.e. before we can detect significant nucleus deformation. We thus believe that nucleus deformation may contribute to their expression, but it is unlikely that we would find a clear-cut contribution of nucleus deformation on the expression of these genes, since they are

already highly expressed when nuclei become more deformed. Instead, the analysis of chromatin status appears more convincing, and also better fits with the idea that mechanical stress would have a more global role on the structural component of the nucleus, i.e. nucleoskeleton and chromatin, rather than an instructive role on specific genes. These new data are important as they establish a link between growth-derived patterns of compression in tissue to nucleus shape and chromatin status.

Further studies would be required to elucidate the structural role of histones, in response to growth-derived forces, in plants. Here we reveal the induction of linker histone H1.3 at the organ-meristem boundary. One may speculate whether H1.3 expression could scale with mechanical stress intensity in different tissues. Interestingly, H1.3 expression has never been detected in the female megaspore mother cell, i.e. in one of the most mechanically protected cells, arguably (32). Yet, we could not detect major phenotypic defects in the H1.3 mutant meristem, at least in control growth conditions (see SI Appendix, Fig. S8). The situation might actually be more complex. Many cross-talks between linker histones have been identified (33), and unsurprisingly, chromatin changes are associated with many pathways, from drought (26) to light (34). Integrating the contribution of mechanical forces in this network is thus likely going to be a long endeavor, but also an exciting one. In particular, this may compel us to see the structural side of chromatin, and analyze the role of the relevant regulators with this lens, also echoing results obtained in animal cells in culture (e.g. (35)).

This work also opens the path to the investigation of the mechanisms leading to such nucleus compression and chromatin compaction. For instance, nuclei may be simply squeezed by pressure, meaning that nuclear density would increase, resulting in chromatin changes. Interestingly, hyperosmotic stress leads to nucleus deformation and chromatin changes in animal cells in culture as well as in isolated nuclei (36). The behavior of nuclei in the cells at the organ-meristem boundary may recapitulate such effects, albeit with mechanically-driven, instead of osmotically-driven, nucleus deformation, and in a growing tissue context. The role of the nuclear envelope is also likely to be important in that pathway (e.g. (37)(38)). In particular, chromatin organization depends on proteins from the Linker of Nucleoskeleton to Cytoskeleton (LINC) complex in plants (39).

In Mammalian cells, stretching was recently proposed to soften chromatin, through a reduction in heterochromatin formation, thereby insulating the genetic material from cellular and supracellular mechanical stress (40). Interestingly, nuclei become stiffer in plant cells through heterochromatin clustering when exposed to hyper-osmotic stress, i.e. when tensile stress level at the cell cortex decreases (41). This could suggest that cortical tension might positively correlate with softer nuclei across kingdoms. Whether this applies to our system remains an open question. The observed reduction in the number of chromocenters at the meristem boundary, both via DAPI staining and mCG-MBD-GFP signal quantification, echoes the behavior of human stem cells placed on stiff environment (42). In our system, such reorganization of chromatin may involve a decrease in individual heterochromatin clusters as well as the spreading of more transient CHH methylation. The accumulation of H1.3 histones would compete with other linker histones (24), but it remains to be shown whether this would also affect nuclear stiffness ultimately.

From a developmental point of view, our work adds another layer of complexity to the definition of the boundary domain in plant shoot apices (19). Beyond morphology (13), hormone signatures (43), gene expression (18), miRNA regulation (44), and stress pattern (10), boundary domains may indeed be also defined by nucleus compression and associated chromatin changes. This likely contributes to its cadastral role and may be conserved beyond the plant kingdom.

Materials and methods

Plant materials and growth conditions

All procedures were performed on plants from the Col-0 ecotype, grown in “long day” conditions, with16hr/8hr light/dark period at 21°C. The *pPDF1::CFP-N7* (20), *pPDF1::mCitrine-MBD* (45), *p35S::SUN1-YFP* (15), *pH1.1::H1.1-EGFP*, *pH1.2::H1.2-EGFP* (32), *pH1.3::H1.3-EGFP* (24), *pHTR5::HTR5-GFP* (46) *pHTR5::mCG-MBD-GFP* and *pHTR5::mCHH-GFP* (30) reporter lines were used for this study.

Meristem dissection

Stems were cut when the SAM switched to an inflorescence meristem identity, i.e. between the appearance of the first flower to the appearance of the first silique (stages 13 to 17, (12)) and transferred on a half MS medium with vitamins and 0.125 µg/µL of BAP for imaging as described in (*11*). Young floral buds were dissected out to access the SAM.

Meristem compression

p35S::SUN1-YFP and *pH1.3::H1.3-GFP* line were grown *in vitro* on a medium containing 10 µM napthylphthalamic acid (NPA, Sigma) as described in (47). As soon as naked inflorescences had formed, the plants were transferred to medium without inhibitor. Within 48 hours, plants were placed in a microvice (see SI Appendix, Fig. S1A). The two blades of the microvice were brought closer so as to induce a strong deformation of the shoot apex. Images were acquired with an upright Leica SP8 or Zeiss LSM700 microscope, as described below (n>5).

DAPI staining of the whole-mount meristems

Prior to staining, the dissected SAM samples were fixed 10 min on ice and then under vacuum (3 times 20 min at room temperature) in a fixing solution containing PBS 1x, EGTA 0.5M, DMSO 10% Formaldehyde 4%. The samples were then dehydrated in ethanol-methanol series as follows: 1x ethanol 70% for 5min, 1x ethanol 100% for 5min, 2x methanol 100% for 5min, 2x ethanol 100% for 5min, and incubated overnight in ethanol 100% at 4°C. Rehydration was performed as follows: 1x ethanol 100% for 5min, 1x ethanol 70% for 5min in PBSt (1% Tween20 in PBS), 1x ethanol 50% for 5min in PBSt, 1x ethanol 30% for 5min in PBSt, and 3x PBSt for 5 mins. Then, the samples were incubated for 30 minutes at 37°C with the mix of cell wall digesting enzymes (48) and RNAse A (0.1mg/ml) and refixed in 4% formaldehyde in PBS. After washing with PBS buffer, the samples were incubated with the DAPI solution (5µg/ml). The mounting of the samples was performed as described in (48).

Confocal laser scanning microscopy and image analysis

Dissected shoot apical meristems from greenhouse plants or naked meristems from *in vitro*-grown NPA-treated seedlings were imaged with a water-dipping lens (x25, NA = 0.8) using an

upright SP8 confocal microscope (Leica, Germany) to generate stack of optical sections with an interval of 0.15 µm between slices. The membranes were stained with FM4-64. All original confocal data is available via the University of Cambridge Data Repository (https://doi.org/xxx link available upon acceptance). Images are presented using the Fire lookup table (ImageJ). Image analysis for chromocenter and CG-methylated regions detection was performed using the 3D object counter option in Fiji software (http://fiji.sc/wiki/index.php/Fiji). The nuclear average signal density was calculated following along the line of the protocol, described in (31). In this case, the mean signal values were normalized to the maximal projected area of the corresponding nuclei and then correlated with their aspect ratio. Statistical analysis was performed using either Microsoft Excel or R software. The two-tailed Student test was performed to compare the means of independent biological sample groups.

Computational Methods

Segmentation

Surface extraction, 2D cell segmentation and Gaussian curvature quantification were performed for the membrane channel (FM 4-64) of the confocal stack images, using the level set method (LSM) package following a published protocol ((49) http://forge.cbp.ens-lyon.fr/redmine/projects/lsm3d) in MorphoGraphX software ((16) https://www.mpipz.mpg.de/MorphoGraphX).

For 3D segmentation of the epidermal layer of cells and corresponding nuclei, an in house script using the MARS/ALT algorithms was developed (50). The confocal images were processed by cropping and applying Gaussian smoothing and alternating sequential filter (ASF). The resulting images were segmented using a watershed algorithm with automatic seeding (50)(17). The segmentation was done for both the membrane channel (FM 4-64) and the nuclear marker channel (*p35S::SUN1-YFP*) of each image. Computed seeds from the membrane channels were used also for the segmentation of the nuclei signal. Cells of the epidermal cell layer were extracted by identifying cells neighboring the image background (the region outside the tissue), which itself was defined as the largest segmented region of the image (17).

Cell labels resulting from the two (MGX and MARS) segmentations were aligned by importing the MARS segmented stack into MGX and applying the manual label transfer followed by application of the Lineage Tracking function.

Cell lineage tracking

To compute cell lineages, affine transformation and subsequently nonlinear transformation were computed to register consecutive confocal images of the membrane-marked channel using the Block-matching framework (50)(51). To compute cell lineages, the computed nonlinear transformation was applied to the corresponding segmented images and optimal cell pairings between registered segmented image and reference segmented image were computed by identifying maximally overlapping cell labels from the two images.

Tissue region extraction

The analysis was performed on epidermal nuclei that were all classified as belonging to the meristem, the organ, or the boundary region in between. The classification was based on the quantified surface curvature of the cells, where the boundary region was defined by cells having negative curvature, as in (52). The rest of the nuclei were classified as meristem or organ depending on which side they were found of a fitted curve along the boundary (Fig. S2A).

Cell and nuclei size and shape quantification

For each segmented object (cell or nucleus), the z-slice with the largest area was extracted for further analysis. The aspect ratio was calculated as the length of the main axis divided by the length of the minor axis of the ellipse representing the covariance matrix of the pixel positions for the region. All properties were extracted using the Matlab function *regionprops*.

Software/protocol

Scripts required to do the segmentation and quantitative analysis are provided via the Sainsbury Laboratory GitLab repository https://gitlab.com/slcu/teamhj/publications/fal_et_al_2021 [publically available upon acceptance], where also a more detailed protocol for executing the steps of the pipeline is provided. All scripts have been developed in Python (https://python.org) and Matlab (MathWorks Inc., Natick, Massachusetts, United States), and the protocol is

dependent on the MorphoGraphX ((16) https://www.mpipz.mpg.de/MorphoGraphX) and MARS/ALT (50) software.

References

1. D. W. Thompson, *On Growth and Form* (Cambridge University press, 1917).
2. T. Lecuit, P.-F. Lenne, E. Munro, Force generation, transmission, and integration during cell and tissue morphogenesis. *Annu. Rev. Cell Dev. Biol.* **27**, 157–184 (2011).
3. B. Hampoelz, T. Lecuit, Nuclear mechanics in differentiation and development. *Curr. Opin. Cell Biol.* **23**, 668–675 (2011).
4. P. Isermann, J. Lammerding, Nuclear mechanics and mechanotransduction in health and disease. *Curr. Biol. CB* **23**, R1113-1121 (2013).
5. H. Q. Le, *et al.*, Mechanical regulation of transcription controls Polycomb-mediated gene silencing during lineage commitment. *Nat. Cell Biol.* **18**, 864–875 (2016).
6. A. Tajik, *et al.*, Transcription upregulation via force-induced direct stretching of chromatin. *Nat. Mater.* **15**, 1287–1296 (2016).
7. S. Pagliara, *et al.*, Auxetic nuclei in embryonic stem cells exiting pluripotency. *Nat. Mater.* **13**, 638–644 (2014).
8. B. Aigouy, *et al.*, Cell flow reorients the axis of planar polarity in the wing epithelium of Drosophila. *Cell* **142**, 773–786 (2010).
9. N. Hervieux, *et al.*, A Mechanical Feedback Restricts Sepal Growth and Shape in Arabidopsis. *Curr. Biol.* **26**, 1019–1028 (2016).
10. O. Hamant, *et al.*, Developmental patterning by mechanical signals in Arabidopsis. *Science* **322**, 1650–1655 (2008).
11. A. Burian, *et al.*, A correlative microscopy approach relates microtubule behaviour, local organ geometry, and cell growth at the Arabidopsis shoot apical meristem. *J. Exp. Bot.* **64**, 5753–5767 (2013).
12. D. R. Smyth, J. L. Bowman, E. M. Meyerowitz, Early flower development in Arabidopsis. *Plant Cell* **2**, 755–767 (1990).
13. D. Kwiatkowska, J. Dumais, Growth and morphogenesis at the vegetative shoot apex of Anagallis arvensis L. *J. Exp. Bot.* **54**, 1585–1595 (2003).
14. M. Louveaux, J.-D. Julien, V. Mirabet, A. Boudaoud, O. Hamant, Cell division plane orientation based on tensile stress in Arabidopsis thaliana. *Proc. Natl. Acad. Sci. U. S. A.* **113**, E4294-4303 (2016).
15. K. Graumann, J. Runions, D. E. Evans, Characterization of SUN-domain proteins at the higher plant nuclear envelope. *Plant J.* **61**, 134–144 (2010).
16. P. Barbier de Reuille, *et al.*, MorphoGraphX: A platform for quantifying morphogenesis in 4D. *eLife* **4**, 05864 (2015).
17. L. Willis, *et al.*, Cell size and growth regulation in the Arabidopsis thaliana apical stem cell niche. *Proc. Natl. Acad. Sci. U. S. A.* **113**, E8238–E8246 (2016).
18. C. Tian, *et al.*, An organ boundary-enriched gene regulatory network uncovers regulatory hierarchies underlying axillary meristem initiation. *Mol. Syst. Biol.* **10**, 755–755 (2014).
19. M. Aida, M. Tasaka, Genetic control of shoot organ boundaries. *Curr. Opin. Plant Biol.* **9**, 72–77 (2006).
20. B. Landrein, *et al.*, Mechanical stress contributes to the expression of the STM homeobox

gene in Arabidopsis shoot meristems. *eLife* **4**, e07811 (2015).
21. K. Fal, B. Landrein, O. Hamant, Interplay between miRNA regulation and mechanical stress for CUC gene expression at the shoot apical meristem. *Plant Signal. Behav.*, 0 (2015).
22. Y. A. Miroshnikova, M. M. Nava, S. A. Wickström, Emerging roles of mechanical forces in chromatin regulation. *J. Cell Sci.* **130**, 2243–2250 (2017).
23. E. A. Booth-Gauthier, T. A. Alcoser, G. Yang, K. N. Dahl, Force-Induced Changes in Subnuclear Movement and Rheology. *Biophys. J.* **103**, 2423–2431 (2012).
24. K. Rutowicz, *et al.*, A Specialized Histone H1 Variant Is Required for Adaptive Responses to Complex Abiotic Stress and Related DNA Methylation in Arabidopsis. *Plant Physiol.* **169**, 2080–2101 (2015).
25. R. Ascenzi, J. S. Gantt, Molecular genetic analysis of the drought-inducible linker histone variant in Arabidopsis thaliana. *Plant Mol. Biol.* **41**, 159–169 (1999).
26. R. Ascenzi, J. S. Gantt, A drought-stress-inducible histone gene in Arabidopsis thaliana is a member of a distinct class of plant linker histone variants. *Plant Mol. Biol.* **34**, 629–641 (1997).
27. F. Tessadori, *et al.*, Large-scale dissociation and sequential reassembly of pericentric heterochromatin in dedifferentiated Arabidopsis cells. *J. Cell Sci.* **120**, 1200–1208 (2007).
28. T. H. Bestor, The DNA methyltransferases of mammals. *Hum. Mol. Genet.* **9**, 2395–2402 (2000).
29. A. Bird, DNA methylation patterns and epigenetic memory. *Genes Dev.* **16**, 6–21 (2002).
30. M. Ingouff, *et al.*, Live-cell analysis of DNA methylation during sexual reproduction in *Arabidopsis* reveals context and sex-specific dynamics controlled by noncanonical RdDM. *Genes Dev.* **31**, 72–83 (2017).
31. M. Versaevel, T. Grevesse, S. Gabriele, Spatial coordination between cell and nuclear shape within micropatterned endothelial cells. *Nat. Commun.* **3**, 671 (2012).
32. W. She, *et al.*, Chromatin reprogramming during the somatic-to-reproductive cell fate transition in plants. *Dev. Camb. Engl.* **140**, 4008–4019 (2013).
33. K. Rutowicz, *et al.*, Linker histones are fine-scale chromatin architects modulating developmental decisions in Arabidopsis. *Genome Biol.* **20**, 157 (2019).
34. C. Bourbousse, F. Barneche, C. Laloi, Plant Chromatin Catches the Sun. *Front. Plant Sci.* **10**, 1728 (2020).
35. K. Damodaran, *et al.*, Compressive force induces reversible chromatin condensation and cell geometry–dependent transcriptional response. *Mol. Biol. Cell* **29**, 3039–3051 (2018).
36. J. D. Finan, F. Guilak, The effects of osmotic stress on the structure and function of the cell nucleus. *J. Cell. Biochem.* **109**, 460–467 (2010).
37. C. Guilluy, *et al.*, Isolated nuclei adapt to force and reveal a mechanotransduction pathway in the nucleus. *Nat. Cell Biol.* **16**, 376–381 (2014).
38. J. Swift, *et al.*, Nuclear Lamin-A Scales with Tissue Stiffness and Enhances Matrix-Directed Differentiation. *Science* **341**, 1240104–1240104 (2013).
39. A. Poulet, *et al.*, The LINC complex contributes to heterochromatin organisation and transcriptional gene silencing in plants. *J. Cell Sci.* **130**, 590–601 (2017).
40. M. M. Nava, *et al.*, Heterochromatin-Driven Nuclear Softening Protects the Genome against Mechanical Stress-Induced Damage. *Cell* **181**, 800–817.e22 (2020).
41. R. Goswami, *et al.*, Mechanical Shielding in Plant Nuclei. *Curr. Biol. CB* **30**, 2013–2025.e3 (2020).
42. A. R. Killaars, *et al.*, Extended Exposure to Stiff Microenvironments Leads to Persistent Chromatin Remodeling in Human Mesenchymal Stem Cells. *Adv. Sci.* **6**, 1801483 (2019).

43. G. Brunoud, *et al.*, A novel sensor to map auxin response and distribution at high spatio-temporal resolution. *Nature* **482**, 103–106 (2012).
44. P. Sieber, F. Wellmer, J. Gheyselinck, J. L. Riechmann, E. M. Meyerowitz, Redundancy and specialization among plant microRNAs: role of the MIR164 family in developmental robustness. *Dev. Camb. Engl.* **134**, 1051–1060 (2007).
45. A. Armezzani, *et al.*, Transcriptional induction of cell wall remodelling genes is coupled to microtubule-driven growth isotropy at the shoot apex in Arabidopsis. *Dev. Camb. Engl.* **145** (2018).
46. H. Wollmann, *et al.*, Dynamic Deposition of Histone Variant H3.3 Accompanies Developmental Remodeling of the Arabidopsis Transcriptome. *PLoS Genet.* **8**, e1002658 (2012).
47. O. Hamant, P. Das, A. Burian, Time-lapse imaging of developing meristems using confocal laser scanning microscope. *Methods Mol. Biol. Clifton NJ* **1080**, 111–119 (2014).
48. F. Rozier, V. Mirabet, T. Vernoux, P. Das, Analysis of 3D gene expression patterns in plants using whole-mount RNA in situ hybridization. *Nat. Protoc.* **9**, 2464–2475 (2014).
49. A. Kiss, *et al.*, Segmentation of 3D images of plant tissues at multiple scales using the level set method. *Plant Methods* **13**, 114 (2017).
50. R. Fernandez, *et al.*, Imaging plant growth in 4D: robust tissue reconstruction and lineaging at cell resolution. *Nat. Methods* **7**, 547–553 (2010).
51. G. Michelin, *et al.*, Spatio-temporal registration of 3D microscopy image sequences of Arabidopsis floral meristems. *IEEE 13th Int. Symp. Biomed. Imaging*, 1127–1130 (2016).
52. T. Stanislas, *et al.*, A phosphoinositide map at the shoot apical meristem in Arabidopsis thaliana. *BMC Biol.* **16**, 20 (2018).

Acknowledgments:

We thank Célia Baroux, Fred Berger, Katja Graumann, and Daniel Grimanelli for providing material used in this article. We are grateful to Grégoire Malandain for the use of Block-matching software. We thank Platim for help with imaging. We also thank Adrienne Roeder for insightful suggestions on this manuscript.

Funding:

This work was supported by the European Research Council (ERC-2013-CoG-615739 ‘‘MechanoDevo’’), Human Frontier Science Program grant RGP0009/2018, the Schlumberger Foundation for Education and Research, CNRS (mécanobiologie « NEstress ») and the Gatsby Charitable Foundation (GAT3395-PR4B).

Author contributions:

K.F., H.J and O.H. conceived and designed the experiments. K.F., and M.L. performed the experiments. N.K., J.T. and Y.R. developed the image analysis pipeline and performed the analysis of nucleus shapes. M-E.C. contributed important protocols and tools. K.F., H.J. and O.H. wrote the manuscript with inputs from all co-authors.

Competing interests:

Authors declare no competing interests.

Data and materials availability:

All original confocal data is available via the University of Cambridge Data Repository (https://doi.org/xxx link available upon acceptance). Scripts for the analysis pipeline are available via the Sainsbury Laboratory GitLab repository (https://gitlab.com/slcu/teamhj/fal_etal_2020 link publically available upon acceptance).

Figure legends

Fig. 1. Nucleus compression at the organ-meristem boundary in Arabidopsis

(**A**) Upper panel shows the maximal projections of confocal stack images with representative dissected shoot apex containing the fluorescent reporters for nuclei (*pPDF1::CFP-N7*, shown in grey), microtubules (*pPDF1::mCitrine-MBD*, shown in yellow), and membranes stained with the FM4-64 (magenta). Lower panel focuses on the boundary domain of representative shoot apex, showing cropped organ and boundary region of the respective sample. Scale bars, 20µm. (**B**) Diagram, representing the top and orthogonal views of a meristem (M) with a growing organ (O). Organ growth laterally pulls (blue arrows) and radially compresses (red arrows) cells at the boundary. (**C**) Representative images of a growing organ at the shoot apex of *p35S::SUN1-YFP* reporter line, acquired at 4 time points within 36 hours. Upper panels display the top view projections and the orthogonal sections of the respective stacks the growing organ and the

boundary domain; the bottom panel displays close-ups in the boundary region where the nuclei (marked with an asterisk) become more elongated following the 36 hours. Green: SUN1-YFP, grey: cell membranes stained with the FM4-64. Scale bars, 10µm, for nuclei at the boundary - 5µm.

Fig. 2. Quantitative nucleus morphometry at the organ-meristem boundary

(A) Quantification of nuclear aspect ratio (upper panel) and local tissue curvature (lower panel) at the boundary region of a growing organ. The nuclear segmentation is performed on the confocal stack images of a representative organ at the meristem, acquired through the 36-hour period. The spatial heatmap plots illustrate the convex hulls of each nucleus, filled with colors to represent the indicated data. The highest values of the nuclear aspect ratio (upper panel) and the local tissue curvature (lower panel) are shown in black; the lowest values of the nuclear aspect ratio the local tissue curvature - in yellow. **(B)** Nuclei at the boundary domain with the highest aspect ratio changes within the acquisition period. (**C**) Plots illustrate the changes in aspect ratio (left), and local tissue curvature (right) of the selected nuclei, highlighted in (B) during the 36 hours observation.

Fig. 3. Expression of linker histones at the SAM

(**A**) Maximal projections of the confocal stacks, showing the expression patterns of the linker histone reporter lines for H1.1, H1.2 and H1.3 at the shoot apex (upper panel) and a close-up in the organ boundary area (lower panel). Scale bar, 20µm. (**B**) Representative naked meristems from *in vitro* NPA-grown *pH1.3::H1.3-GFP* seedlings, as viewed from the top, with or without lateral compression with a microvice. t=0h is the timepoint when the meristem is placed between the blades of the microvice with (bottom) or without (top) compression. Note that the blades of the microvice appear partly fluorescent in the green channel, while a debris can be spotted on top of the meristem in the autofluorescence channel (bottom panels). Scale bar, 50µm.

Fig. 4. Chromatin changes in compressed nuclei at the organ-meristem boundary

(**A,B**) Maximal projection of the confocal stacks showing the expression of the *pHTR5::HTR5-GFP* (**A**) and *pHTR5::mCG-MBD-GFP* (**B**) reporter lines with the global top view (left panels) and close-up in the organ boundary area (right panels). Scale bar, 20µm. (**C**) Representative

pHTR5::mCG-MBD-GFP and *pPDF1::CFP-N7* patterns in organ and meristem domains. Scale bar, 5µm. (**D**) Number of mCG regions in the nuclei correlates negatively with nuclear aspect ratio. Left panel shows violin plots, illustrating the distributions of mCG regions in the nuclei with the aspect ration below 1.55 (n=256) and above 1.55 (n=51). The black line in the violin plot represents the median, the dots are the values of individual samples; *p*-value < 0.05 (*p*-value = $7.3x10^{-5}$, n=5 meristems). Right panel shows a plot of the average number of mCG regions in the nuclei as a function of nuclear aspect ratio. The error bars represent the Standard error of the mean, where 9≤n≤93. (**E**) Left panel shows the violin plot of average nuclear signal density in the nuclei with the aspect ratio below 1.55 (n=331) and above 1.55 (n=74). The black line in the violin plot represents the median, the dots are the values of individual samples; *p*-value < 0.05 (*p*-value = $4.5x10^{-8}$, n=6 meristems). Right panel shows a plot of average nuclear signal density in the nuclei in correlation with the nuclear aspect ratio. The error bars represent the Standard error of the mean, where 19≤n≤133.

Fig. 5. Chromatin changes in compressed nuclei at the organ-meristem boundary in *h1.3* mutant

(**A**) Cartoon drawing illustrating the approach, used for measuring the average nuclear signal density and aspect ratio at the boundary region of a dissected meristem. More precisely, the left panel shows the top and side views of the region between the SAM and a young organ, the L1 layer at the boundary region is shaded in pink with the contours of the nuclei traced. The right panel represents a single nucleus, selected within the target region. The average fluorescence signal is projected from the portion of the z-stack corresponding to the thickness of the cell layer. This data was subsequently used to extract the values of nuclear aspect ratio and average nuclear signal density. (**B**) Plots illustrating the areas (left panel) and aspect ratios (right panel) of the nuclei at the organ boundary regions in WT and *h1.3* mutant plants containing the *p35S::SUN1-YFP* reporter. Sample size for WT: n=201 nuclei from 5 meristems; for *h1.3*: 223 nuclei from 5 meristems. $p\text{-value}_{area}$ = 0.07, $p\text{-value}_{asp.ratio}$ = 0.05. The black line in the violin plots represents the median; the dots are the values of individual samples. (**C**) Violin plot illustration the average nuclear signal density in the WT and *h1.3* nuclei with the aspect ratio below 1.55 (n_{WT}=363, $n_{h1.3}$=473 in 10 meristems for both genotypes) and above 1.55 (n_{WT}=106 and $n_{h1.3}$=106 in 10

meristems for both genotypes). The black line in the violin plots represents the median; the dots are the values of individual samples. Higher average signal density is detected in the nuclei of the WT with the aspect ratio above 1.55 (p-value = 1.35×10^{-5}), compared to below 1.55, a trend not seen in the *h1.3* mutant (p-value = 0.1).

A

Nuclei in the Arabidopsis meristem: general view

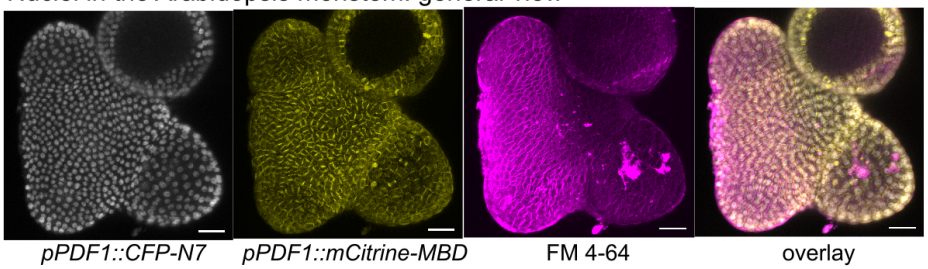

pPDF1::CFP-N7 *pPDF1::mCitrine-MBD* FM 4-64 overlay

Close-up view of the boundary domain

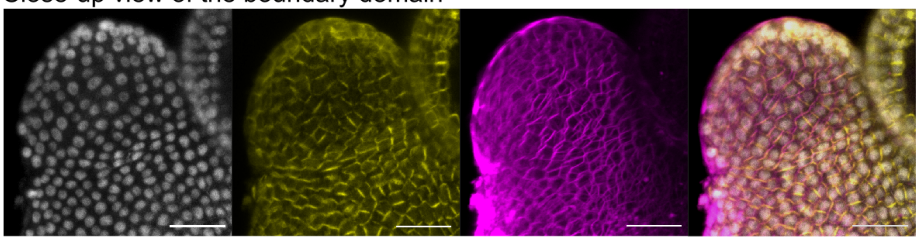

pPDF1::CFP-N7 *pPDF1::mCitrine-MBD* FM 4-64 overlay

scale bar - 20μm

B

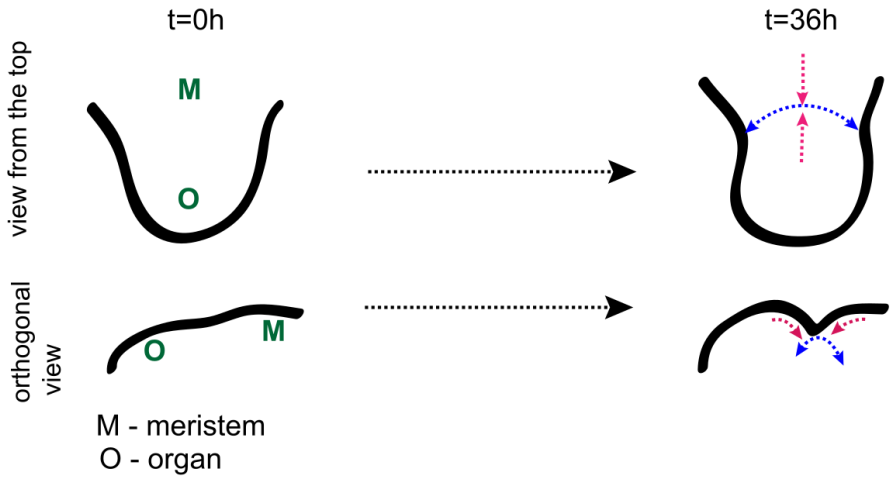

C

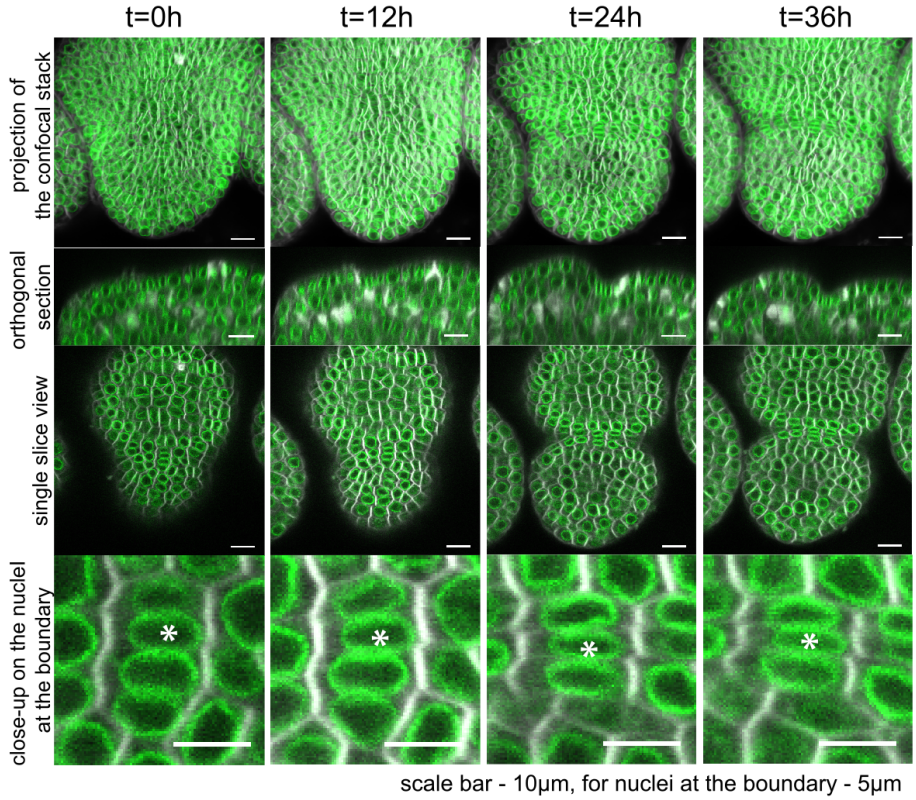

scale bar - 10μm, for nuclei at the boundary - 5μm

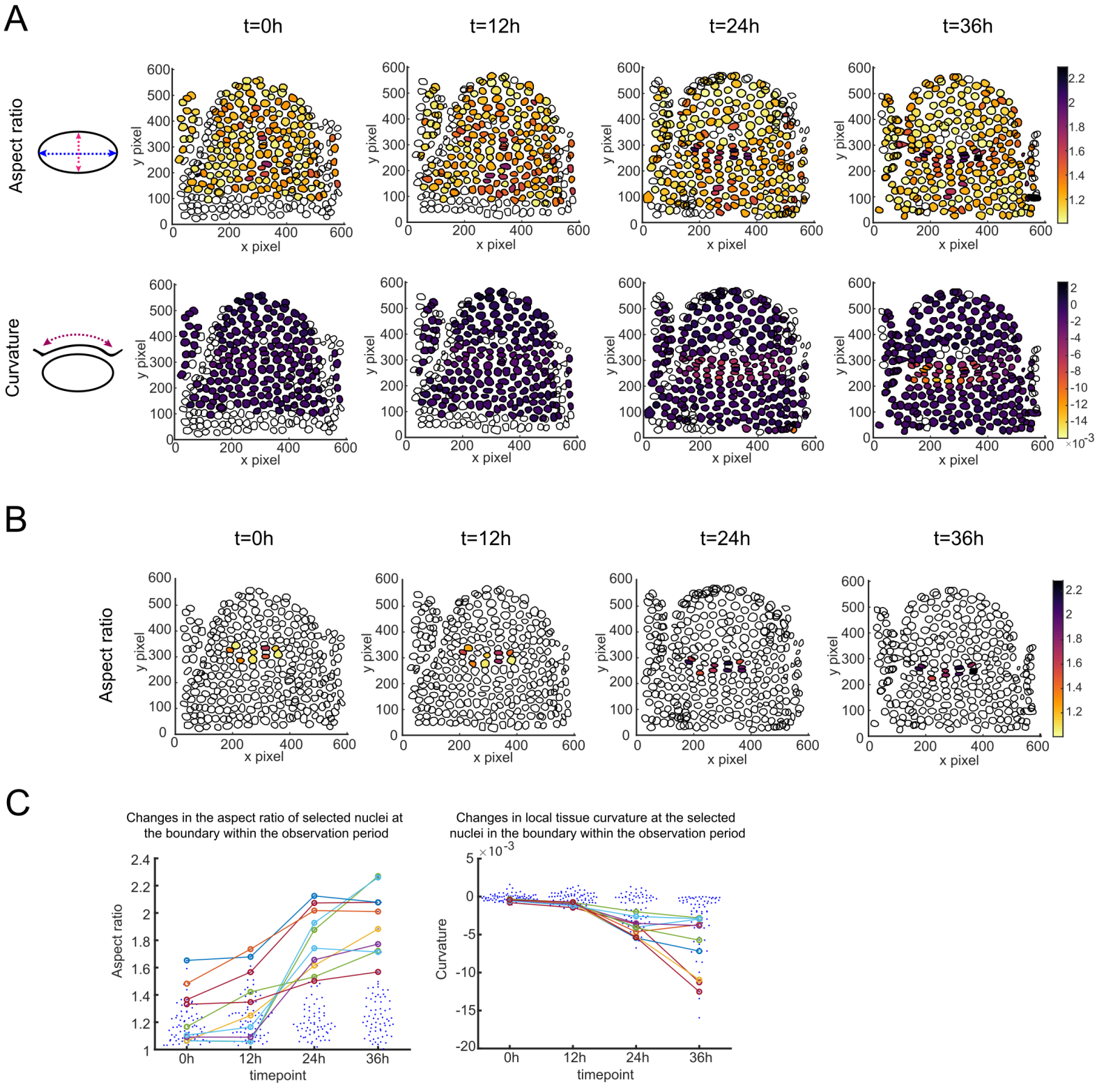
A
t=0h
t=12h
t=24h
t=36h
Aspect ratio
Curvature
y pixel
x pixel
B
C
Changes in the aspect ratio of selected nuclei at the boundary within the observation period
Changes in local tissue curvature at the selected nuclei in the boundary within the observation period
timepoint
0h
12h
24h
36h

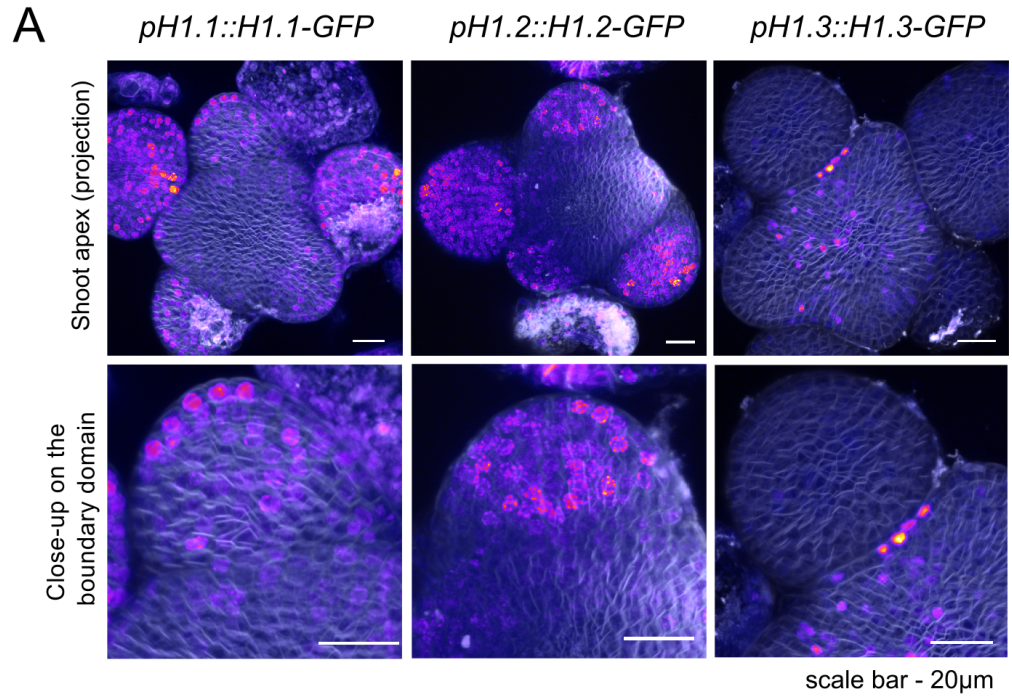
A
pH1.1::H1.1-GFP
pH1.2::H1.2-GFP
pH1.3::H1.3-GFP
Shoot apex (projection)
Close-up on the boundary domain
scale bar - 20µm

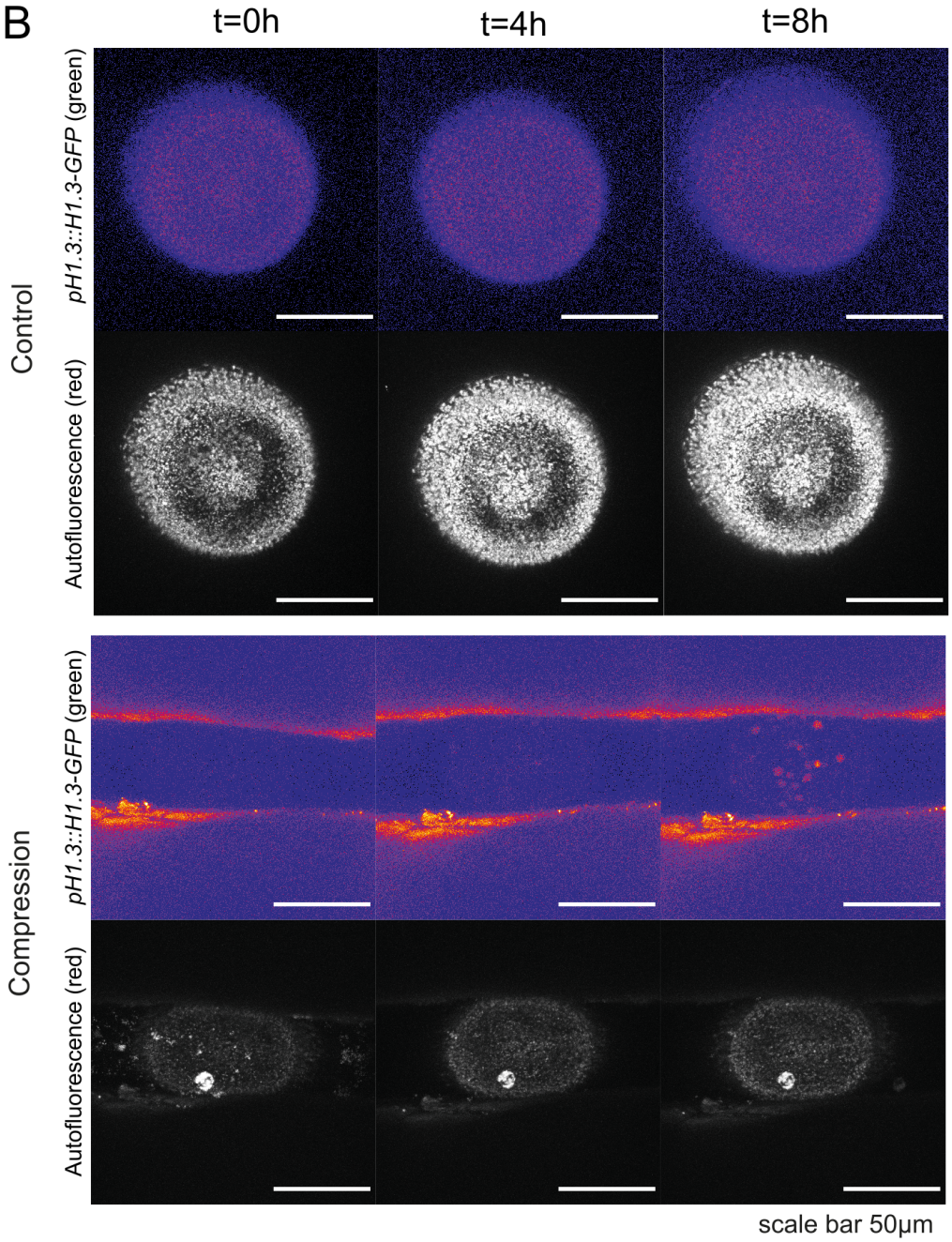
B
t=0h
t=4h
t=8h
Control
pH1.3::H1.3-GFP (green)
Autofluorescence (red)
Compression
pH1.3::H1.3-GFP (green)
Autofluorescence (red)
scale bar 50µm

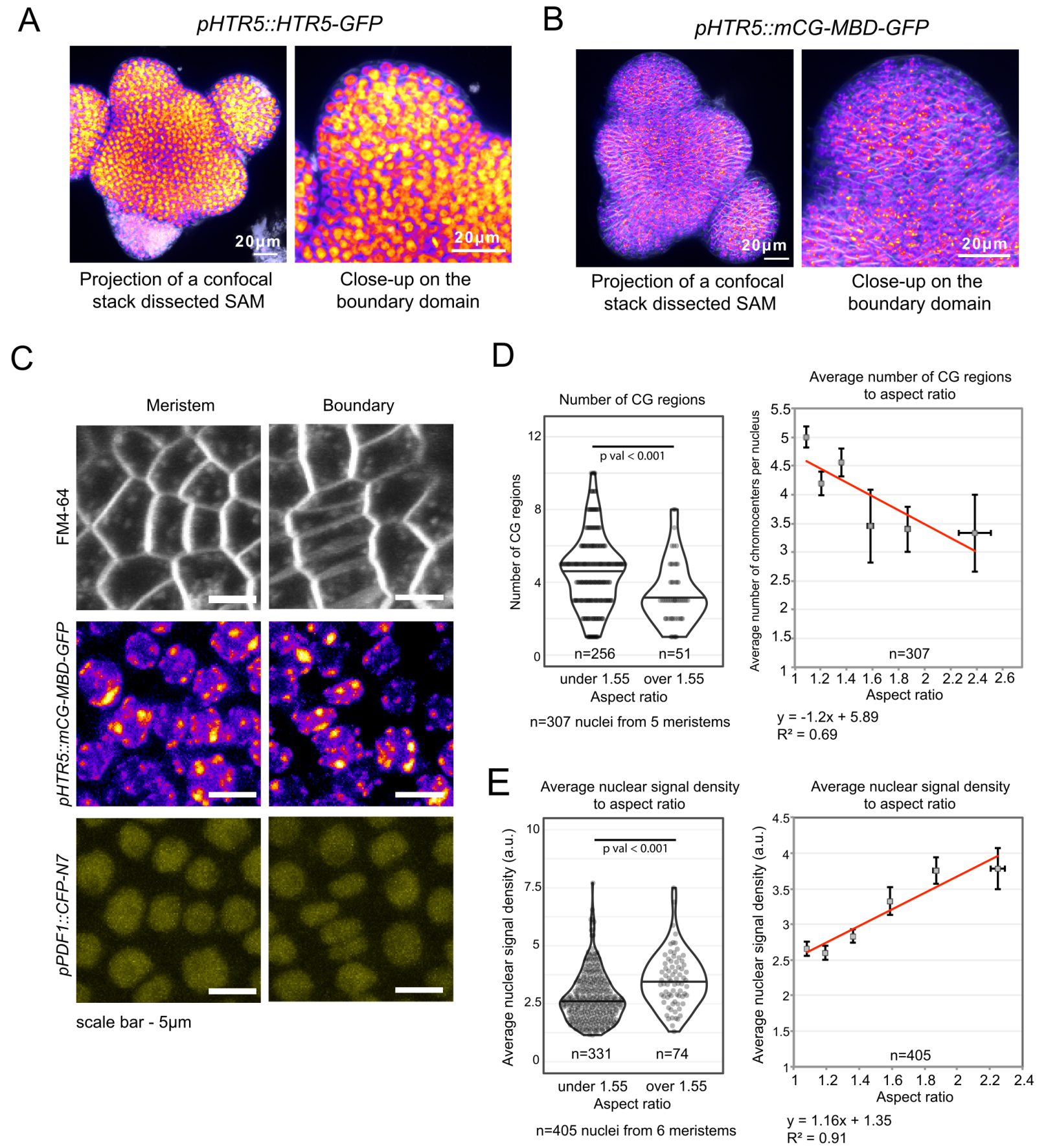
A
pHTR5::HTR5-GFP
20µm
20µm
Projection of a confocal stack dissected SAM
Close-up on the boundary domain
B
pHTR5::mCG-MBD-GFP
20µm
20µm
Projection of a confocal stack dissected SAM
Close-up on the boundary domain
C
Meristem
Boundary
FM4-64
pHTR5::mCG-MBD-GFP
pPDF1::CFP-N7
scale bar - 5µm
D
Number of CG regions
p val < 0.001
Number of CG regions
n=256
n=51
under 1.55
over 1.55
Aspect ratio
n=307 nuclei from 5 meristems
Average number of CG regions to aspect ratio
Average number of chromocenters per nucleus
n=307
Aspect ratio
y = -1.2x + 5.89
R² = 0.69
E
Average nuclear signal density to aspect ratio
p val < 0.001
Average nuclear signal density (a.u.)
n=331
n=74
under 1.55
over 1.55
Aspect ratio
n=405 nuclei from 6 meristems
Average nuclear signal density to aspect ratio
Average nuclear signal density (a.u.)
n=405
Aspect ratio
y = 1.16x + 1.35
R² = 0.91

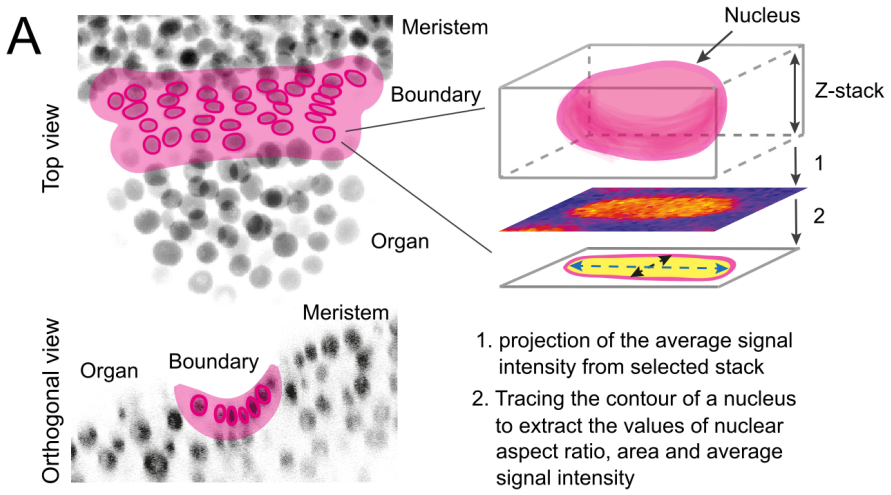
A
Top view
Meristem
Boundary
Organ
Nucleus
Z-stack
1
2
Orthogonal view
Meristem
Organ
Boundary
1. projection of the average signal intensity from selected stack
2. Tracing the contour of a nucleus to extract the values of nuclear aspect ratio, area and average signal intensity

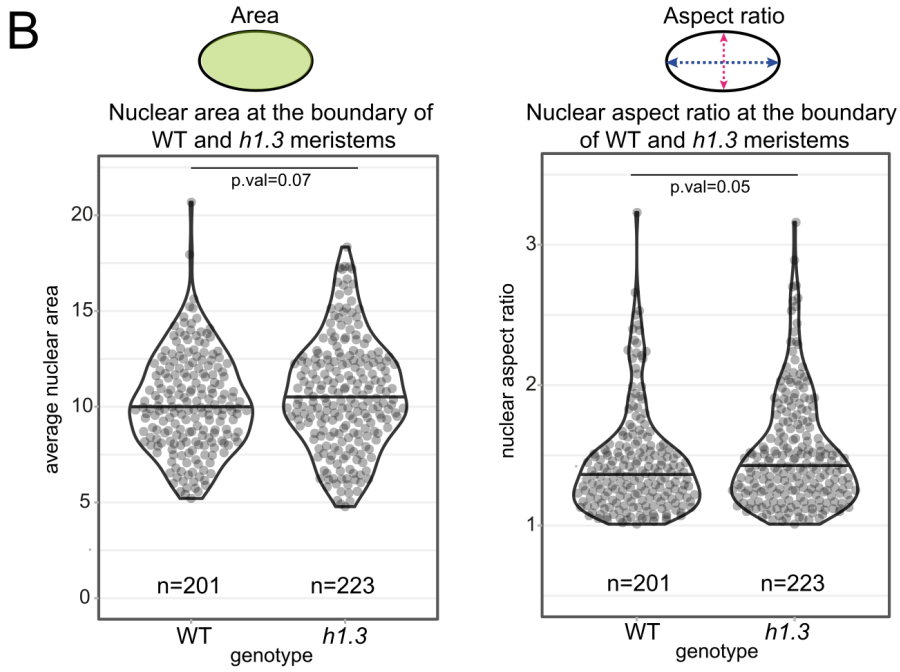
B
Area
Aspect ratio
Nuclear area at the boundary of WT and h1.3 meristems
Nuclear aspect ratio at the boundary of WT and h1.3 meristems
p.val=0.07
p.val=0.05
average nuclear area
nuclear aspect ratio
n=201
n=223
WT
h1.3
genotype

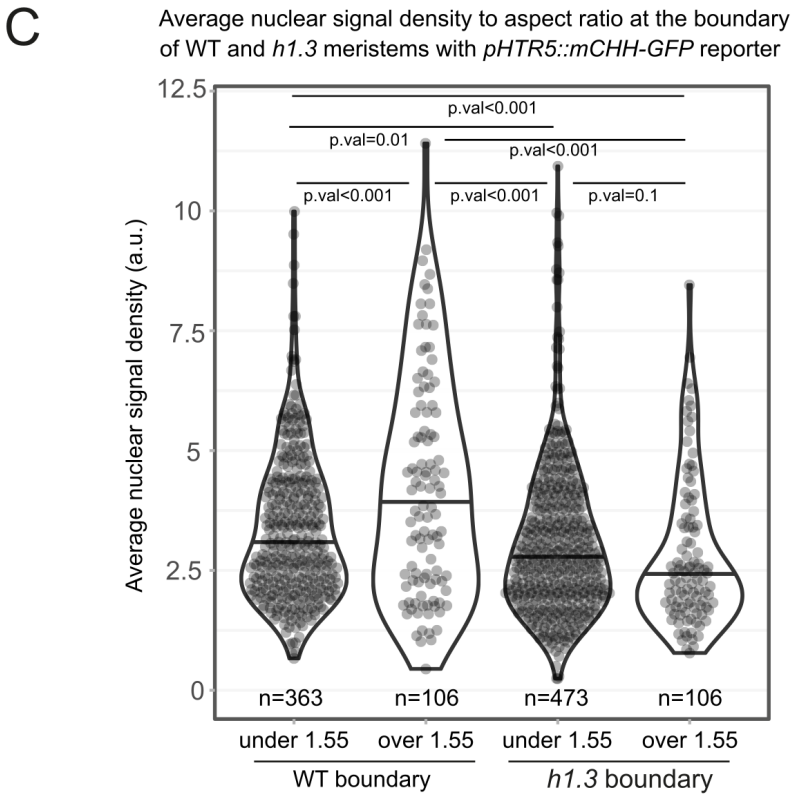
C
Average nuclear signal density to aspect ratio at the boundary of WT and h1.3 meristems with pHTR5::mCHH-GFP reporter
p.val<0.001
p.val=0.01
p.val<0.001
p.val<0.001
p.val<0.001
p.val=0.1
Average nuclear signal density (a.u.)
n=363
n=106
n=473
n=106
under 1.55
over 1.55
under 1.55
over 1.55
WT boundary
h1.3 boundary